Particles I

Access the latest eBook →

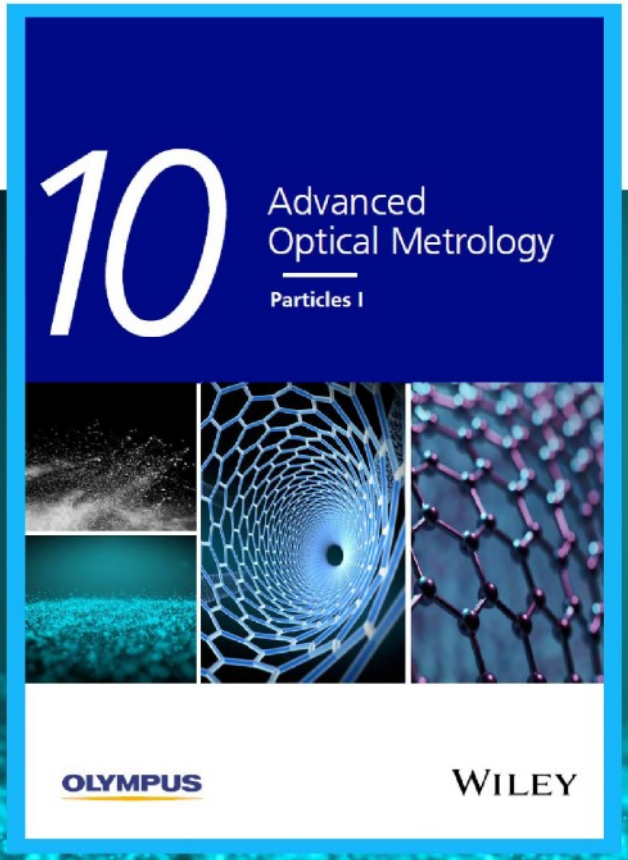

Particles: Unique Properties, Uncountable Applications

Read the latest eBook and better your knowledge with highlights from the recent studies on the design and characterization of micro- and nanoparticles for different application areas.

Access Now

This eBook is sponsored by

OLYMPUS

WILEY

ADVANCED MATERIALS INTERFACES
www.advmatinterfaces.de

Check for updates

Spectroscopic Ellipsometry Investigation of a Sensing Functional Interface: DNA SAMs Hybridization

Giulia Pinto, Silvia Dante, Silvia Maria Cristina Rotondi, Paolo Canepa, Ornella Cavalleri, and Maurizio Canepa*

Here, a comprehensive study of a label-free detection platform for the recognition of oligonucleotide sequences based on hybridization of thiol-tethered DNA strands self-assembled on flat gold films is presented. The study exploits in-buffer spectroscopic ellipsometry (SE) measurements, a noninvasive method sensitive to monolayer films, supported by surface mass density change measurements (Quartz Crystal Microbalance with Dissipation, QCM-D) obtained under comparable experimental conditions. SE and QCM-D allow monitoring deposition of molecular precursors and DNA chain hybridization. Combining SE measurements with QCM-D data paves the way for quantification of the assay through the possible calibration of SE data. Optical measurements also demonstrate the selectivity and recovery properties of the sensing platform. Broadband SE measurements are interpreted by means of an effective optical model. The model, complemented by information on film thickness (scanning probe nanolithography), and surface composition (monochromatic X-ray Photoemission Spectroscopy, XPS), enables a clear spectral identification of UV DNA resonances and the formation of the thiolate interface with gold. Spectroscopic validation of the hybridization is complemented by employing labeled target strands. The influence of hybridization on UV resonances and optical thickness of the DNA film is discussed in the light of hypochromism, through comparison with QCM-D data.

1. Introduction

Selectivity, sensitivity, fast response, and reversibility are important requisites of biosensors for early diagnosis of diseases or monitoring of therapeutic treatments. Many sensing concepts have been proposed and tested in recent years to achieve this challenging mix. For these purposes, hybrid interfaces, where a self-assembled monolayer (SAM) with the desired biofunctionality is immobilized on an inorganic substrate, represent a versatile, popular platform for effective biosensors.

The impressive development regarding the fabrication of functionalized DNA strands have promoted these kinds of molecules as building blocks for the development of sensing platforms.[1–3] Selective and reversible hybridization between complementary strands can be exploited to detect specific biomarkers, from nucleic acid target sequences (such as miRNA,[4] ctDNA[5] or viral sequences[6]) to proteins, by employing protein-DNA conjugates.[7–10] Clearly, the outbreak of the COVID-19 pandemic has boosted the urgent need for highly sensitive, inexpensive and rapid selective recognition of SARS-CoV-2 sequences and spurred research on DNA-based detection of viral sequences.[11,12]

In this work, we analyze a DNA sensing concept that is implemented through a 3-step process (**Figure 1**). The process is initiated with the self-assembly of single-strand DNA (HS-pDNA, 22 bases) that binds to gold through a linker (hexanethiol, C6). According to well-defined protocols,[13] this SAM is exposed to mercaptohexanol (MCH), a thiol with the same alkyl chain length of the hexanethiol linker. It has been reported that MCH co-adsorption improves DNA film organization[14–17] and increases the efficiency of the final, hybridization step[18,19] that implements the recognition of the target sequence.

Literature presents varieties of methods for the recognition of target sequences through the formation of double-strand DNA (dsDNA). Some approaches involve mass sensitive methods like Quartz Crystal Microbalance (QCM)[20–24] or electrochemical methods.[25–28] Optical methods have been proposed that exploit, among others, colorimetric detection,[29] Surface Plasmon Resonance phenomena (SPR)[22,23,30] or combined plasmonic photothermal effects and localized SPR.[31] SPR, in particular, has been valuably employed to study surface confined DNA hybridization on a system closely related to the one under investigation here.[32]

Among optical methods, Spectroscopic Ellipsometry (SE) can be advantageously employed to track changes in film

G. Pinto, S. M. C. Rotondi, P. Canepa, O. Cavalleri, M. Canepa
OptMatLab
Department of Physics
University of Genova
Genova 16146, Italy
E-mail: cavalleri@fisica.unige.it
S. Dante
Materials Characterization Facility
Istituto Italiano di Tecnologia
Genova 16163, Italy

The ORCID identification number(s) for the author(s) of this article can be found under https://doi.org/10.1002/admi.202200364.

© 2022 The Authors. Advanced Materials Interfaces published by Wiley-VCH GmbH. This is an open access article under the terms of the Creative Commons Attribution-NonCommercial-NoDerivs License, which permits use and distribution in any medium, provided the original work is properly cited, the use is non-commercial and no modifications or adaptations are made.

DOI: 10.1002/admi.202200364

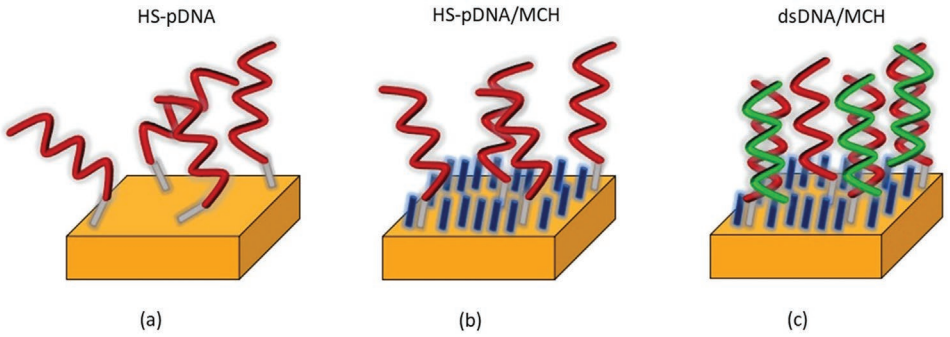

Figure 1. Schematics of the 3-step process: a) probe DNA self-assembly; b) spacer molecule deposition; c) hybridization with target DNA.

thickness.[33,34] With specific regard to transparent ultrathin organic layers, a decrease in the ellipsometric parameter Δ during film formation corresponds to an increase in optical thickness.[35–37] The optical thickness depends on both the film thickness and the complex refractive index of the film. Monitoring Δ in the transparency region of the film therefore provides a viable option for real time monitoring of surface processes and film assembly dynamics.

Indeed, SE can be exploited for a UV–vis–NIR broadband spectroscopic analysis of the sensing system. Simple inspection of the SE data, applying the well-established difference spectra method, may provide some impressive snapshots of film-related processes.[38–44] Modeling of the optical system (substrate/film/ambient) can be performed for a more in-depth interpretation of the data.[36,45] Much useful to feed optical modeling of ultrathin organic films, ancillary analyses such as those based on imaging methods can provide independent estimates of thickness.[46]

Previous Polarization Modulation Infrared Reflection Absorption Spectroscopy studies could identify spectral signatures that allowed to discern between ssDNA and dsDNA.[47] In principle, access to the intense UV absorptions around 260 nm can lead to the detection of other specific spectral fingerprints of DNA adsorption/hybridization processes. In this respect, an attractive aspect concerns the spectral characterization of the hypochromic effect, which is expected upon hybridization.

Indeed, hypochromism, and the reverse hyperchromism in response to dehybridization, are phenomena well known from many studies of DNA in solution. A sharp increase in optical absorption efficiency, up to 30% or even more, is commonly observed after DNA denaturation.[48–51] The origin of the phenomenon is still debated and many models, featuring varying degrees of sophistication, have been devised to explain it.[51] Several state-of-the-art quantum chemistry calculations have examined various factors related to base stacking,[52] intra- and inter-strand delocalization of excitonic states,[53] or long-range interactions between nucleobases.[51]

To the best of our knowledge, this interesting topic has not been ever addressed explicitly for DNA SAMs. We can mention an SE study of DNA immobilized on a silicon surface.[54] The spectral limitation of the experiment on the UV side prevented direct observation of DNA resonances. The authors interpreted their data with basic models and found an increase (5%) of refractive index after hybridization they judged too small, invoking a decrease in polarizability per nucleotide after hybridization that we actually trace back to hypochromia.

For a comprehensive system analysis, optical methods can be advantageously combined with in-situ QCM with Dissipation (QCM-D) measurements. QCM-D measures the changes in the resonance frequency of an oscillating crystal upon film deposition onto its surface. Frequency changes can be converted into an extensive quantity such as deposited mass and provide additional and complementary information on the kinetics of mass changes. For rigid films, the well-known Sauerbrey equation can be applied to convert frequency into mass changes.[55,56] Soft, highly hydrated films exhibiting a viscoelastic behavior are better described by the Voigt modeling.[57] The ratio of dissipation changes to frequency changes ($\Delta D/\Delta f$) can provide further insight into the rigid versus viscoelastic behavior of the film, high values of the ratio being indicative of soft viscoelastic films.[23]

The synergy between SPR and QCM-D [58,23] and between SE and QCM-D [24,35,59–61] measurements has already been demonstrated, and will display its broad potential also in our experiments. Further, QCM-D measurements may represent a valuable liaison to those research works which use mass change detection as the primary method to detect recognition.[62]

We report here a useful concept for the design of label-free DNA biosensors, which couples optical spectroscopy measurements, aimed at probing the interaction between complementary strands, and the detection of film thickness (or density) change. In our approach, in-situ SE measurements with single-layer sensitivity are proposed as a viable tool for both purposes.

We accurately studied the recognition of the target strand through the hybridization process. We have tested the selective recognition of target sequences using complementary strands, including labeled molecules, as well as not complementary strands. Denaturation/renaturation cycling was carried out to verify the recovery of the platforms. The effect of hybridization-induced hypochromism on SE difference spectra is discussed.

While the paper focuses on the sensing step, the preparation of the SAM precursor to hybridization is a somewhat delicate point. Following previous works,[63–65] X-rays Photoelectron Spectroscopy (XPS) was performed to add chemical specific information regarding the molecule-substrate interface with attention to the modifications induced by co-adsorption of MCH.

The SE dataset, along with its analysis and interpretation, complemented by QCM-D, AFM and XPS, provides a consistent picture of the various processes involved and illustrates the strengths and weaknesses of the concept.

© 2022 The Authors. Advanced Materials Interfaces published by Wiley-VCH GmbH

2. Results and Discussion

2.1. Monitoring Hybridization: Real Time Measurements

Representative QCM-D measurements are shown in **Figure 2**a (see SI.1 in the Supporting Information for the evaluation of the molecular assembly time constants). Figure 2b shows in-situ SE dynamic measurements, the time evolution of Δ measured at 800 nm, obtained under comparable conditions. The injection of each molecular solution produces a sudden change in QCM-D and SE signals which keep stable after rinsing with TE buffer, indicating that deposited molecules are strongly bound to the surface as expected for thiolated molecules (HS-pDNA, MCH) on gold or for target DNA (tDNA) hybridized with its complementary DNA anchored on gold (HS-pDNA).

Regarding QCM-D data, the low values of dissipation (see inset of Figure 2a), as well as the close superposition of the different overtone signals (see Figure S2, Supporting Information) and the rather low $\Delta D/\Delta f$ ratio values, are indicative of rigid, low hydrated films.[57]

In particular, our system is characterized by $\Delta D/\Delta f$ values of $\approx 25 \times 10^{-9}$ Hz^{-1} for both steps of HS-pDNA self-assembly and hybridization with tDNA. Higher $\Delta D/\Delta f$ values, of 60 10^{-9} Hz^{-1} and 72 10^{-9} Hz^{-1}, have been reported for single strand and hybridized DNA films anchored to the QCM quartz crystal through biotin/avidin coupling.[23] Even higher $\Delta D/\Delta f$ values can be derived from studies on DNA strands coupled to supported lipid bilayers.[24,58] Such high $\Delta D/\Delta f$ values, are indicative of a viscoelastic film behavior. Thus, the dissipative behavior of the DNA films appears to be related to the film/substrate coupling. The direct coupling of the DNA strands to the gold surface via a short thiol linker used in the present study likely results in the formation of dense, quite rigid films with a low water content. This finding is in agreement with a previous study on thiolated DNA films that were actually described as rigid films.[35]

Thus, we applied the Sauerbrey equation[55,56] to convert changes in frequency to deposited mass (right axis in Figure 2a), as detailed in the Experimental Section.

From QCM-D data, we have been able to estimate the evolution of molecular density on the gold-coated quartz following sequential deposition of HS-pDNA, MCH, and target tDNA.

Exposure to HS-pDNA leads to a mass increase of about 600 ng cm^{-2}. As detailed in SI.1.2 (Supporting Information), from the mass increase, one can obtain the molecular surface density and the average nearest-neighbor distance. The resulting surface molecular density, 5.3×10^{13} molecule cm^{-2}, is in agreement with previous electrochemical,[66,67] optical[19] and X-ray spectroscopy (XPS)[63,64,68] studies. Modeling the SAM as a closely packed hexagonal layer, the molecular density provides an average nearest-neighbor distance of 15 Å, in good agreement with previous reports.[67]

The increase in mass following exposure to MCH (average value 80 ng cm^{-2}) gives a molecular density of 4.1×10^{14} molecule cm^{-2} for the mixed HS-pDNA/MCH SAM, with an average nearest-neighbor distance of 5.3 Å, in very good agreement with compact alkanethiol SAMs.[69] This finding indicates that MCH fills the empty binding sites in the low density HS-pDNA SAM, leading to a molecular reorganization within the film as confirmed by lateral force AFM imaging (see SI.2, Supporting Information). Final exposure to the target DNA solution produces an increase of mass (average value 260 ng cm^{-2}) corresponding to a tDNA molecular density of 2.3×10^{13} molecule cm^{-2}, in agreement with previous reports.[19,70] The molecular density of the target DNA is about half the density of the probe DNA, indicative that one out of two DNA probes are hybridized by the target DNA. The nearest-neighbor distance between target DNA strands calculated from the measured molecular density turns out to be 2.2 nm, a value that matches well the expected 2 nm diameter of a DNA double helix.[71] This finding suggests that hybridization leads to the formation of a quite dense layer of double helix DNA, implying a steric limitation for the 2:1 pDNA:tDNA hybridization ratio.

As reported in Figure 2b, also SE Δ data show a well-defined sequence of three transitions, each step-down indicating an increase in optical thickness. The absolute value of changes is very small, that suggests a limited optical contrast between the film and the ambient, throughout the whole experiment.

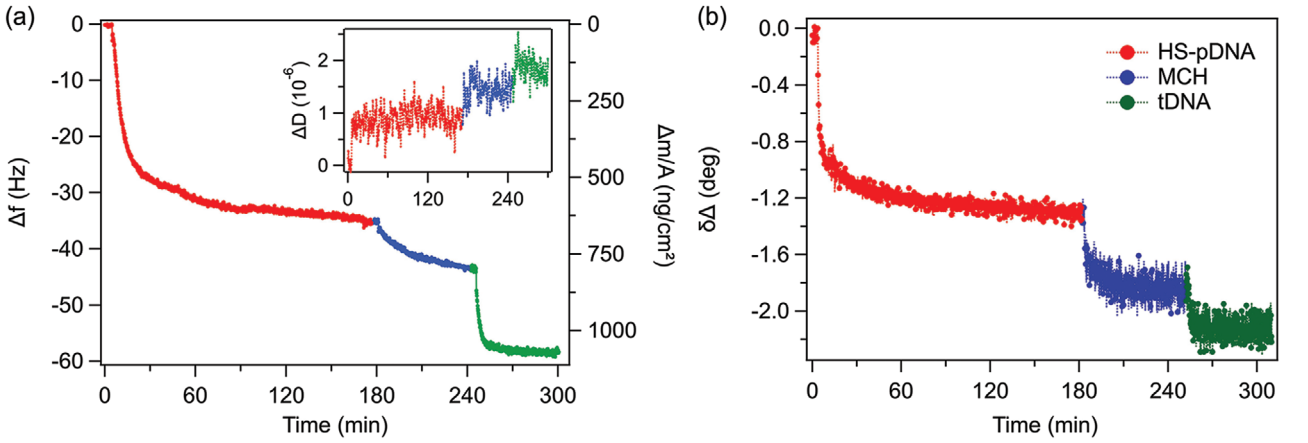

Figure 2. Dynamics of dsDNA/MCH film self-assembly: HS-pDNA + MCH + tDNA. a) Frequency variation (7th overtone) (left axis) and mass/area ratio variation (right axis) (QCM-D experiment). Inset: dissipation variation versus time. b) Δ variation at 800 nm (SE experiment).

© 2022 The Authors. Advanced Materials Interfaces published by Wiley-VCH GmbH

Quick examination of QCM-D and SE data shows that the magnitude of the Δ jumps is not "proportional" to the magnitude of the jumps observed in QCM. The increase of mass (and molecular density) detected by QCM, for the hybridization stage, seems not matched by a jump of the "equivalent" entity of optical thickness. A difference between QCM mass uptake and "optical mass" response is conceivable due to the different sensitivity to water entrapped in the film.[23]

The SE dynamics data can no longer be interpreted by simple changes in film density or thickness and observed variations most likely reflect the morphologic and structural evolution of the overlayer. At the angle of incidence set by the cell geometry, the way the light probes the film depends on the interplay between the refractive index of ambient, molecular layer and substrate; in particular the optical contrast of organic film and ambient changes during successive depositions and related reactions. Note that for highly hydrated brush layers in an aqueous environment, under particularly unfavorable conditions, it could be even hard to observe part of the film.[41] More insight into the evolution of SE data required analysis of broadband measurements.

2.2. Spectral Insight on Hybridization

2.2.1. Broadband Ellipsometry Analysis

"Static" SE measurements were performed when steady state conditions were reached as evidenced by the dynamic measurements. In this regard, it is worth mentioning that steady-state Δ values remain substantially stable after rinsing with TE buffer. To emphasize the SAM contribution to the SE static measurements, difference spectra were analyzed, referenced to the gold substrate spectra as detailed in section Spectroscopic Ellipsometry. **Figure 3** reports SE static difference spectra for HS-pDNA, HS-pDNA/MCH, and dsDNA/MCH SAMs (SE spectra used to calculate the difference spectra in Figure 3 are reported in Figure S5, Supporting Information). Each phase of the experiment leads to quasi-rigid decrease of $\delta\Delta$ broadband spectral values ($\delta\Delta_{3/0} < \delta\Delta_{2/0} < \delta\Delta_{1/0}$). Decrease of $\delta\Delta$ in the NIR limit is consistent with a sequential increase of the optical thickness.[37] The values, comparable with those obtained for other in-situ investigations on biomolecules,[36] are altogether very small over the whole spectral range, confirming the limited optical contrast between film and ambient.

Nevertheless, one can appreciate general trends typical of difference spectra of SAMs on gold.[37] In particular, $\delta\Delta$ spectra present a relative maximum at the high reflectivity threshold of gold, around 500 nm (Figure 3a) where $\delta\Psi$ curves exhibit a well-defined downward transition from positive to negative values (Figure 3b).[40,72]

In contrast with the behavior of transparent films,[38] narrow spectral features with a deep minimum/maximum can be observed in $\delta\Delta$ and $\delta\Psi$ curves, respectively, toward the UV end of the spectra.

We have observed similar narrow features in many experiments on organic and biological films endowed with optical absorptions in the visible and near UV range.[39,42,36,45,72] These features, which can be neatly observed in both in-situ and ex-situ experiments, are representative of the variation of the complex index of refraction across the frequency of molecular resonances.[36] Here, as detailed later on, we assign these features to the UV absorptions of DNA, which are observed in transmission measurements in solution peaked at 260 nm (inset in Figure 3b).[36,73] At first glance, the UV "dips" exhibit poor variations across the three steps of the experiment. In Figure S6 (Supporting Information), a close up of $\delta\Delta$ and $\delta\Psi$ in the UV region and vertical shifts of the curves help the comparison. A closer look to these spectra suggests a modest broadening and perhaps a small redshift of the dip after hybridization. Similar effects were reported in an earlier study on hypocromism.[74]

The three $\delta\Psi$ spectra (Figure 3b) differ substantially above 500 nm. Negative NIR $\delta\Psi$ values are related to the formation of a nanoscale interface layer resulting from the chemical bond of molecules with the substrate, as it is the case of thiolate[38] and selenolate[40] SAMs on gold.

$\delta\Psi_{2/0}$ (blue, mixed film) NIR data are more negative than $\delta\Psi_{1/0}$ (red, HS-pDNA). Relying on previous research on related

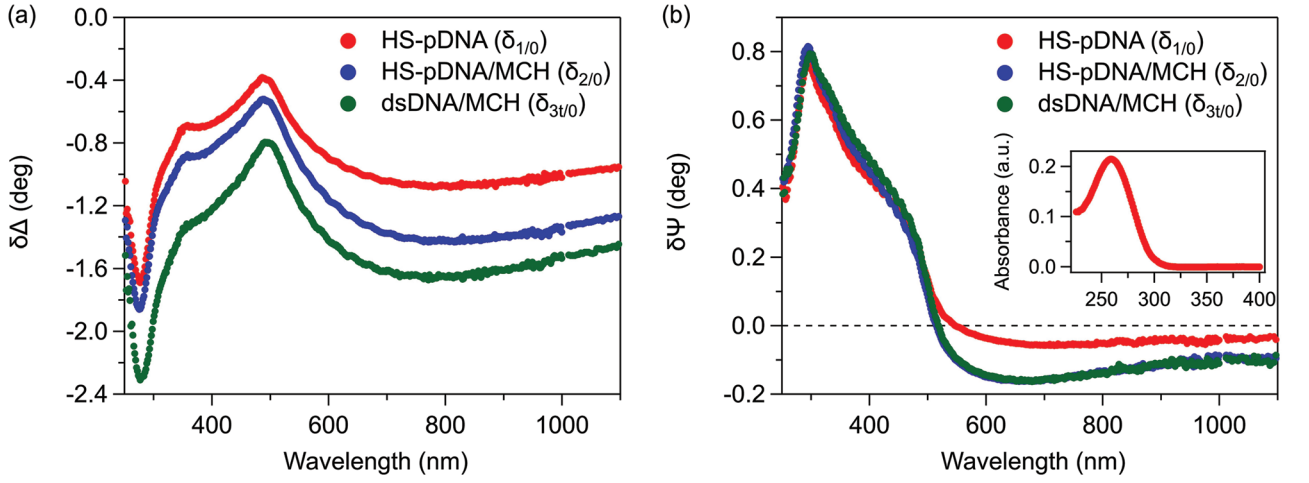

Figure 3. a) $\delta\Delta$ and b) $\delta\Psi$ spectra of HS-pDNA (red curve), HS-pDNA/MCH (blue curve), and dsDNA/MCH (green curve) SAMs. Inset: absorbance spectrum of HS-pDNA diluted in TE buffer.

© 2022 The Authors. Advanced Materials Interfaces published by Wiley-VCH GmbH

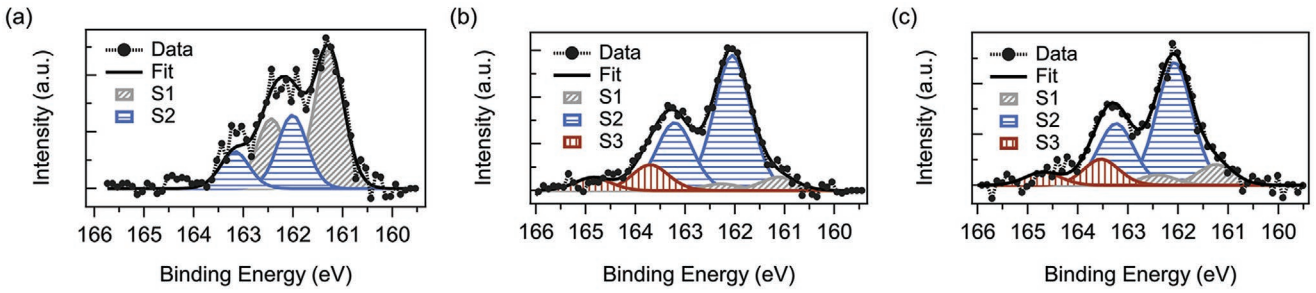

Figure 4. S2p XPS spectra acquired on samples a) incubated in HS-pDNA solution, b) exposed to MCH, and c) hybridized with tDNA.

systems,[38] this behavior indicates a modification of the film/Au interface. In this respect, note that the incubation in tDNA does not affect the NIR behavior further. Conceivably, the interaction of tDNA with its complementary immobilized DNA probe does not affect the molecule/substrate interface.

The interpretation of the trend of NIR $\delta\Psi$ data considering the formation of the thiolate interface found further justification after investigating the S-Au bond properties by XPS measurements. The comparison between representative S2p core level spectra of HS-pDNA, HS-pDNA/MCH, and dsDNA/MCH films is reported in **Figure 4**.

Regarding HS-pDNA (panel a) the spectra present two doublets (FWHM = 0.7 eV): S1, with the main $2p_{3/2}$ component (161.3 ± 0.2) eV Binding Energy (BE) and a lower intensity one, S2, at (161.8 ± 0.2) eV BE.

In XPS experiments on well-organized alkanethiols SAMs[75–80] on Au (111) terraces, S2p doublets with the $2p_{3/2}$ component around 162 eV BE are usually assigned to so-called strongly bound species.[81–83]

The origin of S2p signals in the range 161–161.5 eV BE, like S1, is more debated.[84] Some reports assigned states detected in this energy range to thiol molecules binding to gold atoms with coordination different from S2, possibly due to chemisorption on steps or kinks,[85,86] while other authors suggested that chemistry rather than surface sites determines the binding energy of the S2p core level region.[87] S1 states have been also tentatively assigned to the cleavage of C-S bond after irradiation or annealing [88–82] or to atomic sulfur.[90]

After incubation in MCH (Figure 4b), the S2p core level region dramatically changes. The S2 component becomes largely dominant and S1 substantially vanishes.

The chemisorption of the short-chain thiol competes successfully with S1-like DNA species. MCH adsorption can affect the mobility of gold atoms thereby promoting some local reorganization of the interface with changes in molecule/gold coordination and transition to the S2 state.

Note that a third, low intensity component, S3, is observed, with the $2p_{3/2}$ component at 163.5 eV, assigned to so-called unbound thiol groups.[83,84,91] States related to oxidized sulfur at about 167–168 eV BE were not detected.

The large MCH-induced change in the S2p spectrum thus parallels the evident increase in the negative $\delta\Psi$ part in the NIR. Relatively large, negative NIR $\delta\Psi$ are most likely associated to the increase of the surface density of S2 bonds, confirming previous experiments on other, simpler thiols.[72]

After hybridization, the S2p region does not present significant evolution, in consistence with the outcomes of NIR $\delta\Psi$ ellipsometry measurements.

Other relevant molecular related core level regions (C1s, O1s, N1s, and P2p signals) are reported in Figure S7 (Supporting Information). The spectra do not present significant differences regarding peak positions between HS-pDNA, HS-pDNA/MCH and dsDNA/MCH films. The ratios between the intensities of the C, O, N, P signals and the S signal decrease after incubation in MCH, due to the increased number of sulfur atoms, while increase after the hybridization step, due to the increment of C, O, N and P atoms in the film composition (see Table S2, Supporting Information).

2.2.2. Optical Model for DNA SAMs

We have built a reasonably simple optical model, based on stacked layers coupled by Fresnel boundary conditions, to interpret the main features of broadband difference spectra.

Let us premise that so-called three-layer (substrate/film/ambient) or even four-layer (substrate/interface/film/ambient) models, especially for transparent films, have proven ineffective to reproduce experimental data from UV to NIR. Four-layer model simulations for transparent films (Figure S8, Supporting Information) fail totally in the UV, while perform relatively well above 400 nm, far from the DNA absorptions, thus giving indicative estimates of the NIR refractive index and film thickness.[73]

A stack of five layers is necessary to account for the complex vertical morphology of the film. The five layers comprise (**Figure 5**):

- SUBSTRATE. The optical constants were obtained by inversion of the spectra of bare Au thick film samples,[34] as done in several previous papers.[73]
- INTERFACE. An effective transition layer.
- SPACER. This layer represents the effect of alkylic linker and MCH molecules. It is transparent (real refractive index) throughout the investigated frequency range.[39]
- DNA FILM. This layer represents DNA strands with their UV absorptions.
- AMBIENT. An aqueous ambient, simulated by a Cauchy layer with $A_{ambient}$ = 1.33; $B_{ambient}$ = 0.0028 μm^2; $C_{ambient}$ = 0.00005 μm^4 (values based on results of J. R. Krivacic[92] and taking into account a 1 M NaCl buffer concentration[93]).

© 2022 The Authors. Advanced Materials Interfaces published by Wiley-VCH GmbH

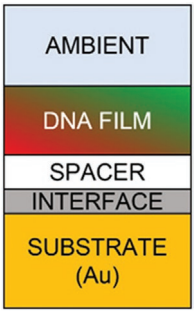

Figure 5. Scheme of the five-layer model.

For the SPACER, INTERFACE, and DNA FILM layers, we have adopted simple models, limiting the number of adjustable parameters as much as possible in order to reduce the chance of overmodeling. Following this approach, and again considering the small thickness of the film, we have chosen to ignore anisotropy effects [45] which have been identified in relatively thick DNA films deposited by evaporation.[94,95]

We focused simulations on ssDNA/MCH and dsDNA/MCH SAMs, for which it is conceivable to assume a dense SPACER layer with "standing-up" molecules.[19,66]

Regarding the SPACER we have opted for a very basic model, assuming a constant refractive index (in practice, discarding dispersion in the Cauchy equation, $n(\lambda) = A + \frac{B}{\lambda^2} + \frac{C}{\lambda^4}$).

The dielectric function of the INTERFACE layer was then modeled applying the well-known effective medium approximation Bruggeman formula (BEMA), which "mixes" the dielectric functions of SUBSTRATE and SPACER according to the volume fractions of the two components (i.e., $f_{\text{Spacer}} + f_{\text{Substrate}} = 1$).[96]

This approach proved effective to obtain the negative $\delta\Psi$ values in the NIR region for thiolated SAMs on gold.[38]

The SPACER "decouples" the SUBSTRATE from the DNA FILM, and eliminates the possibility that the INTERFACE dielectric function retains trace of the DNA UV absorptions, a problem that arises in four-layer models.[40]

The DNA FILM dielectric function was taken as

$$\varepsilon = P(\omega) + G(\omega) + \varepsilon_{1\infty} \tag{1}$$

$P(\omega)$ is a so-called Pole, an oscillator without broadening ($P = \frac{A_{Pole}}{E_{Pole}^2 - E^2}$), which accounts for far UV absorptions of DNA, outside of the investigated spectral region (around 190 nm).[97,98]

$G(\omega)$ is a superposition of oscillators that shape the relatively narrow spectral structures in the accessible UV region. The imaginary part of $G(\omega)$ is written by summing appropriate Gaussians

$$\varepsilon_{2G} = \sum_i \left(A_i * e^{-\left(\frac{E-E_i}{\sigma_i}\right)^2} - A_i * e^{-\left(\frac{E+E_i}{\sigma_i}\right)^2} \right) \text{ with } \sigma_i = \frac{B_i}{2\sqrt{\ln 2}} \tag{2}$$

where A_i (dimensionless), E_i (eV) and B_i (eV) denote the amplitude, the energy position, and the broadening of the ith oscillator, respectively.

The $\varepsilon_{1\infty}$ offset essentially determines the (real) value of refractive index in the NIR limit, much less affected by Gaussian resonances and the pole. Since we deal with ultrathin and relatively low-index films, $\varepsilon_{1\infty}$ exhibits a marked degree of correlation with film thickness.

To mitigate index-thickness correlation issues we have chosen to set the sum of the SPACER thickness and the SPACER-bound fraction of the INTERFACE layer to the estimated length of a C6 alkyl chain, i.e., $d_{\text{Spacer}} + d_{\text{B-EMA}} * f_{\text{Spacer}} = d_{\text{C6}}$ assuming $d_{\text{C6}} = 0.6$ nm.[39]

Finally, we resorted to AFM-nanolithography measurements (Figure S3, Supporting Information) which provide independent film thickness data, according to a method, so called nanoshaving,[46] applied in previous work on other organic films.[37,41,73] In short, using appropriate AFM tips and operating procedures, small pits of regular shape and contour are dug into the film reaching down to the substrate. The AFM itself is then exploited to measure accurately the depth of the holes, which gives a good approximation of the overlayer (SPACER+DNA FILM) thickness. Once set the thickness of the SPACER, the thickness of the DNA FILM follows consequently.

The analysis of nanoshaving data provided the values of (3.5 ± 0.6) nm and (5.0 ± 0.6) nm for HS-pDNA/MCH and dsDNA/MCH SAMs thickness, respectively. The error bars account for the uncertainty associated with the measurement and the variability observed across different pits and samples.

Figure 6a–d shows a comparison between data and model calculations that helps explain the influence of the parameters and put refractive index/thickness correlation in proper perspective.

The dotted curves have been selected by fitting data above 500 nm while the Gaussian parameters were tuned to seek the best reproduction of position, intensity, and width of UV resonance-like features in both $\delta\Psi$ and $\delta\Delta$ data. Two relatively broad Gaussian oscillators, at 261 and 277 nm, proved sufficient to account for the narrow UV dips. The position of the two oscillators is in general agreement with the literature; the lowest energy state likely represents the π–π^* transition.[99]

Table 1 lists the parameter values associated with the simulations for HS-pDNA/MCH (dotted curves in Figure 6a,b) and dsDNA/MCH (dotted curves in Figure 6c,d) SAMS. Corresponding real and imaginary parts of the DNA FILM refractive index derived from simulations are shown in Figure 6e,f.

In Figure 6a–d, two more simulations (continuous curves dark gray), that differ from the dotted curve only in the value of $\varepsilon_{1\infty}$, graphically identify an area (light gray shading) that "bounds" the experimental data below 500 nm. The NIR refractive index corresponding to these simulations is indicated in Figure 6a–d.

For both sets of data, the NIR refractive index, about 1.40–1.42 (Figure 6e,f), is somewhat below values reported in the literature for thicker "dry" DNA films.[54,100] This is not surprising as the measurements have been performed in liquid.

The model overall loses accuracy toward the UV region. The inaccuracy is likely connected to the level of approximation that is inherent to the simple, isotropic stacking model, versus the actual complexity of the system. For instance, Bruggeman's effective model for the INTERFACE works well to reproduce

© 2022 The Authors. Advanced Materials Interfaces published by Wiley-VCH GmbH

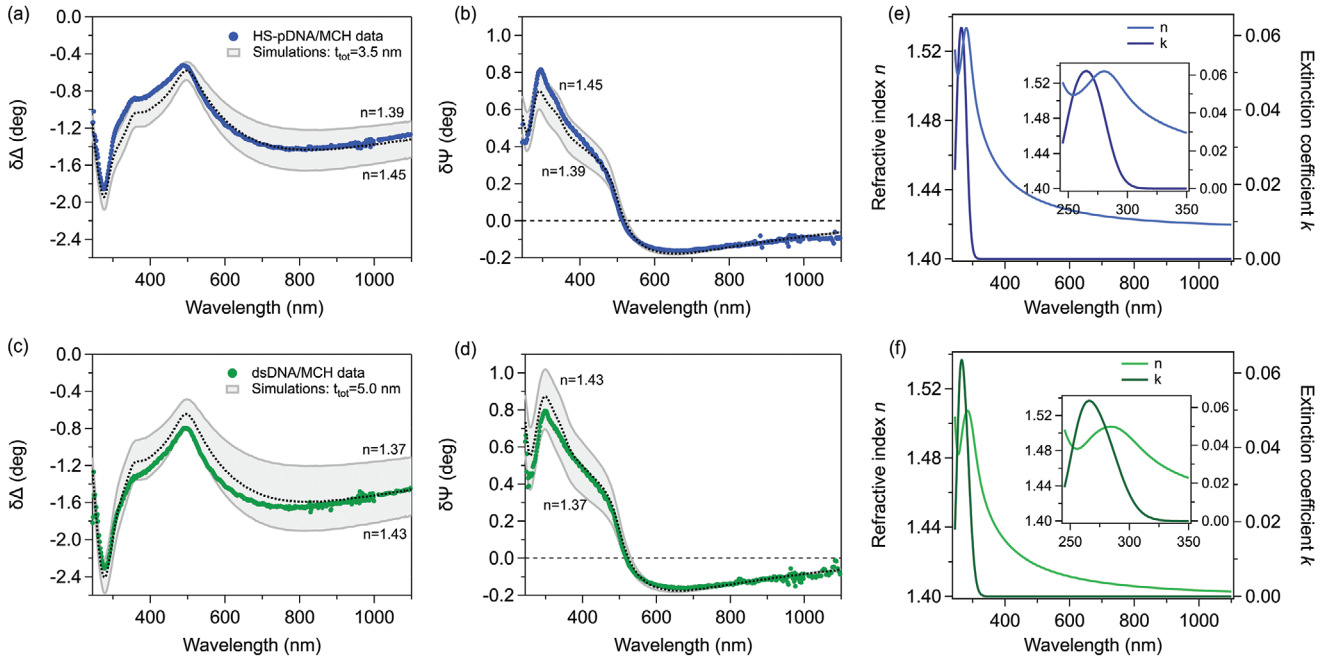

Figure 6. Comparison between SE experimental data (points) and simulations (curves) for DNA films. The simulations have been obtained setting the total film thickness (t_{TOT}) value after analysis of nanoshaving AFM measurements. a,b) HS-pDNA/MCH: $\delta_{2/0}(\Delta)$ and $\delta_{2/0}(\Psi)$ data (blue points), simulations corresponding to t_{TOT} = 3.5 nm and n(1300 nm) = 1.42 (black dotted curves). c,d) dsDNA/MCH: $\delta_{3t/0}(\Delta)$ and $\delta_{3t/0}(\Psi)$ data (green points), simulations corresponding to t_{TOT} = 5.0 nm and n(1300 nm) = 1.40 (black dotted curves). In panels (a)–(d), dark gray curves differ from the dotted one only in the value of $\varepsilon_{1\infty}$ (the corresponding NIR refractive index is indicated). e,f) Refractive index and extinction coefficient corresponding to dotted curves of panels (a)–(d). Model parameters associated with simulations are listed in Table 1.

negative $\delta\Psi$ data in the NIR. However, we cannot exclude that the same model may introduce undesirable effects or even distortions for shorter and shorter wavelengths.[40]

Note that the effective model for the INTERFACE layer affects also the $\delta\Delta$ in the NIR. If we come back to Figure 2(b) and reconsider the data after exposure to MCH molecules (blue data), part of the downward jump should be ascribed to the effect of interface formation and not solely to a thickness/density change.

Table 1. List of parameters employed in the five-layer model.

	HS-pDNA/MCH	dsDNA/MCH
INTERFACE (B-EMA)	t_{EMA} = 0.4 nm, f_{Cauchy} = 80%	
SPACER (Cauchy)	t_{Cauchy} = 0.3 nm	
	A_{Cauchy} = 1.45, B_{Cauchy} = 0 μm^2, C_{Cauchy} = 0 μm^4	
DNA FILM (GenOsc)	t_{GenOsc} = 2.9 nm, $\varepsilon_{1\infty}$ =1.75	t_{GenOsc} = 4.4 nm, $\varepsilon_{1\infty}$ = 1.78
	E_{pole} = 6.29 eV (197 nm)	
	A_{pole} = 9.5	
	E_{G1} = 4.80 eV (258 nm)	E_{G1} = 4.75 eV (261 nm)
	A_{G1} = 0.15, B_{G1} = 0.5 eV	
	E_{G2} = 4.51 eV (275 nm)	E_{G1} = 4.42 eV (281 nm)
	A_{G2} = 0.1	
	B_{G2} = 0.4 eV	B_{G2} = 0.5 eV
$t_{TOT} = t_{EMA}{*}f_{Cauchy} + t_{Cauchy} + t_{GenOsc}$	3.5 nm (from AFM data)	5.0 nm (from AFM data)

Hypochromism in immobilized DNA. As mentioned in the introduction, optical studies of DNA in solution characterized the hybridization-induced hypochromism, by examining the UV spectral transmission. Even more studies reported on hyperchromism in response to denaturation.[48–51] In these experiments, when the double helices melt, the "total" number of strands is conserved.

To our knowledge there are no studies addressing hypochromism/hyperchromism in DNA molecules immobilized at surfaces. Therefore, in principle, our experiments could add information on this attracting phenomenon in a situation different from usual experiments in solution. However, competing issues made it challenging to interpret the observations. On the one hand, the "total" number of strands (and mass as well) on the surface is increased after hybridization events. Under the assumption, discussed in Section 2.1, of moderate hydration of the DNA film, a mass increase up to 40–50%, can be estimated by QCM-D. The larger number of strands should induce a sizable increase in UV absorptions and, consequently, also an increase of the NIR refractive index. On the other hand, hybridization-induced hypochromism goes in the opposite direction, acting to decrease the optical absorption efficiency. Some counterbalance of the two factors can be therefore expected a priori.

In the raw SE data (see also Figure S6, Supporting Information) the spectral features most directly related to the UV absorptions of DNA show little change after the hybridization process, aside from a small broadening, or even a small redshift. Modeling of SE data (see Figure 6e,f with insets) confirms these qualitative observations and would suggest even a small decrease of NIR refraction index after hybridization.

© 2022 The Authors. Advanced Materials Interfaces published by Wiley-VCH GmbH

The number of assumptions made in the SE model, and the overall experimental uncertainties, clearly dictate caution about too tight quantitative determinations; nevertheless, it seems safe to rule out both a neat increase of UV absorptions and an increase in the NIR refractive index after hybridization.

The results thus lead us to assume that, for our films, the loss of optical absorption efficiency (hypochromism) expected from hybridization tends to compensate for the increase in absorption intensity due to the increase in the number of immobilized strands.

2.2.3. Selectivity

In order to provide further spectroscopic proof of the selectivity of surface confined hybridization, we repeated SE experiments using labeled not-complementary (n-tDNA*) and complementary strands (tDNA*).

Figure 7a shows SE dynamic scans (at 800 nm). No change is detected after exposure of HS-pDNA/MCH SAMs to n-tDNA* (orange curve). Static spectra (not shown) confirm the absence of variations in the whole investigated spectral region.[101]

A neat downward transition is instead observed after exposure (of the same sample) to tDNA* (black curve). Figure 7b,c compares the static difference spectra obtained after incubation in tDNA* ($\delta_{3t^*/0}$, black squares) and in tDNA ($\delta_{3t/0}$, green circles), after thorough rinsing in TE buffer.

The tDNA* spectra exhibit spectroscopic signatures of the Atto590 dye (comparison with transmission spectroscopy data in the inset). These features, particularly evident in the $\delta\Psi$ data between 500 and 700 nm, are graphically emphasized in the figures. Lower values of the $\delta_{3t^*/0}(\Delta)$ curve in the NIR region are a consequence of the dye absorptions in the visible and of a small increase of thickness due to the hindrance of the dye. The presence of the dye does not significantly affect the UV region.

Therefore, hybridization experiments with tDNA* add another clear spectroscopic evidence to the occurrence of hybridization between complementary strands.

2.2.4. Reversibility

For the reusability of DNA-based biosensors, the reversibility of the hybridization process is of key importance. After hybridization, we tested the denaturation process exposing the dsDNA/MCH film to 1 M NaOH solution[102] to regenerate the HS-pDNA/MCH surface. Results are shown in Figure 7d. Exposure to the NaOH solution (violet curve) results in a fast increase of Δ, indicating a decrease of the optical thickness; Δ recovers to the prehybridization value once TE buffer is reintroduced into the cell. The hybridization/denaturation cycles have been repeated up to five times showing an unchanged efficiency.

An important issue in terms of biosensor development is the preservation of the selective recognition properties of the sensing platform upon storage in dry conditions. To this end, we checked and successfully verified the occurrence of hybridization and denaturation cycles on HS-pDNA/MCH SAMs upon at least one week storage in dry conditions (see Figure S9, Supporting Information).

3. Conclusions

We presented a comprehensive study of hybridization of monolayers of thiol-tethered ss-DNA self-assembled on flat gold thick films, with assistance of co-deposition of a short-chain thiol spacer. This functional interface is representative of sensing platforms based on DNA-DNA recognition. Surprisingly enough, a comprehensive characterization with broadband optical spectroscopy tools of this sensing platform is still lacking. The paper focuses on the systematic application of in situ spectroscopic ellipsometry measurements. The measurements covered a frequency region from the UV to the NIR and included the region of the DNA absorption band, around 260 nm.

We have exploited the so-called difference spectra approach to seek unlabeled optical validation of hybridization. The optical study has been complemented by other methods that provide important collateral information on key quantities, such as surface mass density change (QCM-D), film thickness (AFM), and surface chemical composition (monochromatic XPS).

A relatively simple optical model, backed by AFM measurements of layer thickness after shaving nanolithography, allowed a reliable interpretation of difference spectra to be achieved. Analysis of the data led to an assessment of the general spectral characteristics related to optical thickness variation, providing a credible estimate of the refractive index of the DNA film in the NIR. It also made possible a clear assignment of narrow spectral features directly related to the UV resonances of the DNA and the formation of the thiolate interface with the substrate.

Analysis of UV absorptions and optical thickness, corroborated by comparison with QCM-D data, allowed discussing the effect of hybridization-induced hypochromism of the DNA absorbers. While hypochromism (or the reverse phenomenon of hyperchromism) has been commonly observed in many types of experiments dealing with molecular solutions, to our knowledge our results represent the first attempt to characterize this interesting phenomenon for DNA monolayers immobilized on a surface.

A careful and critical inspection of the raw difference spectra is sufficient to obtain a first, quick information about hypochromism, even without resorting to time-consuming simulations.

Spectroscopic validation of the hybridization has been complemented by employing target strands labeled with a dye molecule. Beyond the effects relating to hypochromism, the difference spectra showed unequivocally the occurrence of the absorption band of the dye in the visible range.

In addition to allowing real-time monitoring of molecular precursor deposition and DNA chain hybridization, dynamic SE experiments also demonstrated the selectivity and recovery properties of the detection platform.

In conclusion, spectroscopic ellipsometry has proven to be a suitable, nonperturbative method allowing effective monitoring of the sequence recognition process, also in lack of labeling.

© 2022 The Authors. Advanced Materials Interfaces published by Wiley-VCH GmbH

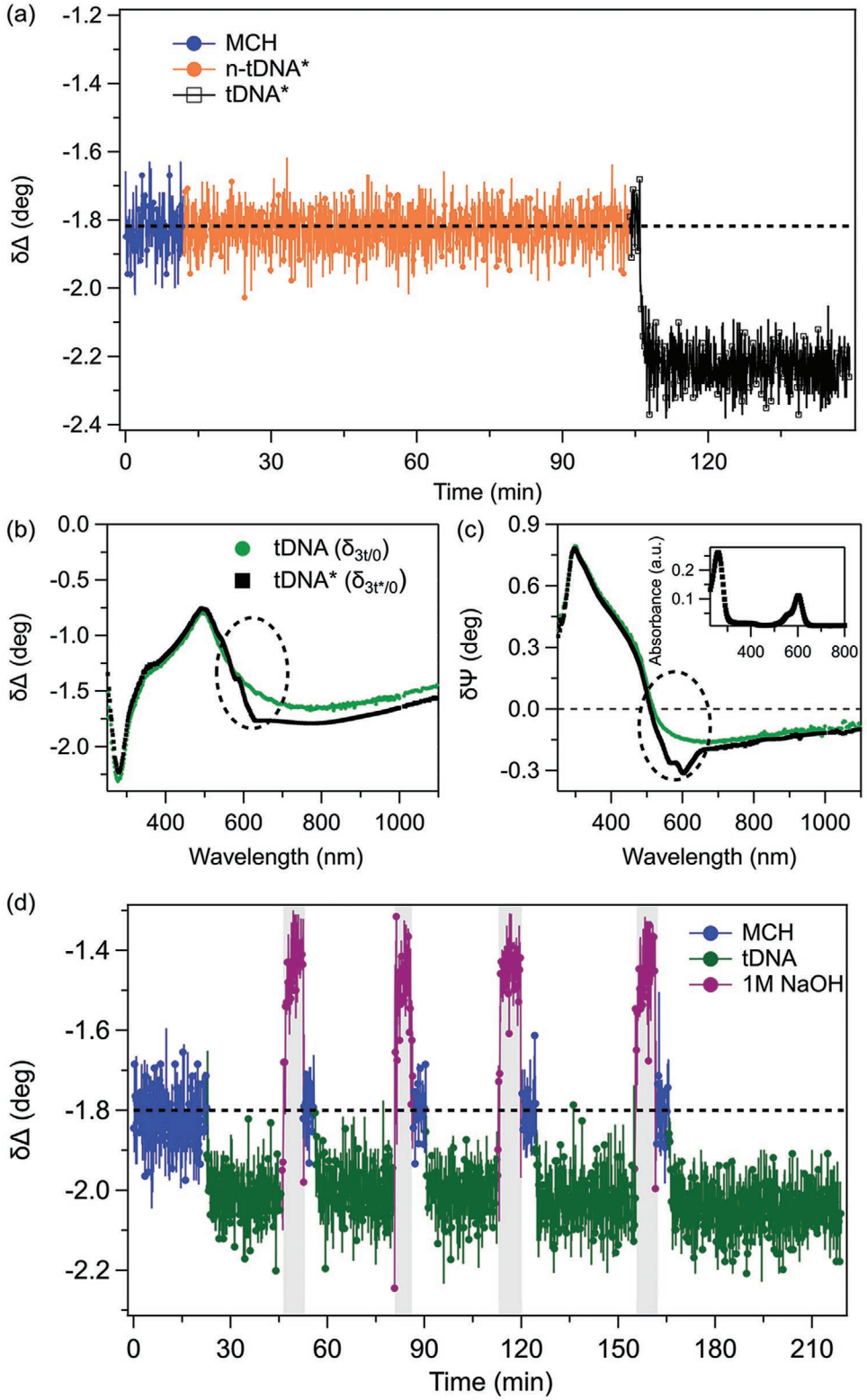

Figure 7. a–c) Selectivity and d) recovery tests. a) Monitoring Δ at 800 nm during incubation of HS-pDNA/MCH film in n-tDNA (data in orange) and tDNA* (data in black). b) $\delta\Delta$ and c) $\delta\Psi$ spectra of dsDNA/MCH respect to the gold substrate after exposure of HS-pDNA/MCH film to tDNA ($\delta_{3t/0}$, green circles) and tDNA* ($\delta_{3t^*/0}$, black squares). For tDNA*, dye absorptions in the visible range are emphasized by dashed loops. Inset: absorbance spectrum of tDNA* in TE buffer. d) Monitoring Δ at 800 nm during cycles of incubation of HS-pDNA/MCH films in tDNA (measurements in TE buffer), followed by denaturation in 1 M NaOH solution (measurements in NaOH solution, gray shading).

© 2022 The Authors. Advanced Materials Interfaces published by Wiley-VCH GmbH

The difference spectra method can be applied independently of the substrate and is also practicable in microspectrometry experiments applied to sensor arrays. Combining SE measurements with QCM-D data obtained under comparable conditions also allows calibration of $\delta\Delta$ data and paves the way for quantification of the assay.

The validation approach described here can be extended to any other sensor platform based on molecular recognition. In particular, applications where accuracy becomes even more important than speed, such as in forensic biomedicine, can benefit from this analysis. Last but not least, the method is useful for providing a solid background of broadband spectroscopy to more agile tools, such as the QCM-D itself, or to give prior support to single-wavelength SPR experiments, which interpretation is only seemingly simpler, yet certainly most popular among bioscientists and in day-by-day practice.

4. Experimental Section

Materials and Reagents: HPLC purified oligonucleotides were purchased from biomers.net GmbH and used as received:

- Probe strand: HS-$(CH_2)_6$-5'-TAATCGGCTCATACTCTGACTG-3' (HS-pDNA)
- Target strand: 3'-CAGTCAGAGTATGAGCCGATTA-5' (tDNA)
- Labelled target strand: 3'-CAGTCAGAGTATGAGCCGATTA-5'-Atto590 (tDNA*) [Atto590: absorption 594 nm, emission 624 nm]
- Labelled no-target strand: 3'-AAAAAAAAAAAAAAAAAAAAA-5'-Atto590 (n-tDNA*)

Tris[hydroxymethyl]amino-methane (Tris base), ethylenediaminetetraacetic acid (EDTA) and 6-Mercapto-1-hexanol (HS–$(CH_2)_6$–OH, MCH) were purchased from Sigma Aldrich. Sodium chloride (NaCl) was purchased from Merck. Sulfuric acid (H_2SO_4) and 30% hydrogen peroxide (H_2O_2) were purchased from Carlo Erba. Aqueous Ammonia 30% (NH_4OH) was purchased from Sigma-Aldrich. All solutions were made with ultrapure deionized water (resistivity ≥ 18 MΩ cm) from a Millipore MilliQ system.

Experiments were performed in TE buffer prepared with 10×10^{-3} M Tris, 1×10^{-3} M EDTA and 1 M NaCl, pH adjusted at 7.2 using HCl (Fluka).

Flat gold substrates purchased from Arrandee were used for SE and XPS measurements.

Gold-coated quartz sensors (Biolin Scientific; resonance frequency: 5 MHz) were used for QCM-D measurements.

Sample Preparation: Arrandee substrates were cleaned with piranha solution (4:1 H_2SO_4:30%H_2O_2) for 3 min, thoroughly rinsed with Milli-Q water and dried under a nitrogen stream (*CAUTION – Piranha should be handled with extreme care: it is extremely oxidizing, reacts violently with organics and should only be stored in loosely tightened containers to avoid pressure buildup*).

Gold-coated sensors for QCM-D measurements were cleaned with basic piranha solution (1:1:5 30% ammonia solution, 30%H_2O_2, ultrapure water) for 5 min at 75 °C, thoroughly rinsed with Milli-Q water, and dried under a nitrogen stream. Sensors were subjected to 10 min UV/Ozone treatment before usage.

XPS and AFM analysis showed that the two cleaning procedures lead to substrates with similar surface properties with respect to cleanness and roughness.

HS-pDNA oligonucleotide self-assembly was carried out by keeping the clean gold substrates in 1×10^{-6} M HS-pDNA solution in TE buffer for 3 h at room temperature (≈22 °C). To improve film organization, samples were then immersed in 5×10^{-6} M 6-Mercapto-1-hexanol solution in TE buffer (ambient temperature, 1 h).[14–17,] Hybridization was performed by exposing the mixed SAMs to the target sequence (1×10^{-6} M tDNA or tDNA* in TE buffer) for 2 h at ambient temperature. Rinsing in TE buffer was performed after each molecular deposition step.

To check for sensor specificity, incubation experiments in no-target DNA were carried out, exposing mixed HS-pDNA/MCH SAMs in a 1×10^{-6} M n-tDNA* solution for 1.5 h at room temperature.

In passing we note that sensitivity test experiments showed appreciable SE signal variations upon exposure to tDNA solutions at concentrations down to a few tens of nM.

Spectroscopic Ellipsometry: Spectroscopic Ellipsometry measurements were performed using a rotating compensator instrument (M-2000, J.A. Woollam Co., 245–1700 nm) equipped with a 75 W Xe lamp. Spectra have been collected in situ using a commercial liquid cell (J.A. Woollam Co., 0.5 mL).

Fused silica windows (Edmund Optics, York, UK (part number 45–308)) with a featureless, 90% transmittance over the probed spectral range were mounted into the liquid cell.

Absorbance measurements of HS-pDNA and dsDNA solutions were performed using a JASCO V-530 UV-VIS Spectrophotometer.

The measurement protocol for "static" and "dynamic" SE experiments was the following:

(I) "static" reference: characterization of gold substrate in TE buffer;
(II) "dynamic" characterization of film formation in the molecular solution; we monitored the effects of exposing the sample to the appropriate reagent (HS-pDNA, MCH and tDNA solutions). During these real-time measurements, the system has been sampled every 7 s for HS-pDNA and every 3.5 s for MCH and tDNA solution.
(III) "static" characterization of the film: substitution of incubation solution with TE buffer and characterization of SAM. In order to emphasize the contribution of the ultrathin organic layer we analyzed difference spectra, i.e., the difference between spectra acquired after the film deposition (Ψ_i,Δ_i) and spectra measured on the bare substrate (Ψ_0,Δ_0) (standard spectra are reported in Figure S5, Supporting Information).[36,41] Difference spectra related to the different deposition steps are referred to as follows:
  (i) after HS-pDNA deposition: $\delta_{1/0}(\Psi, \Delta) = (\Psi_1,\Delta_1) - (\Psi_0,\Delta_0)$;
  (ii) after addition of MCH: $\delta_{2/0}(\Psi, \Delta) = (\Psi_2,\Delta_2) - (\Psi_0,\Delta_0)$;
  (iii) after hybridization with target tDNA: $\delta_{3t/0}(\Psi, \Delta) = (\Psi_{3t},\Delta_{3t}) - (\Psi_0,\Delta_0)$;
  (iv) after incubation in n-tDNA: $\delta_{3n/0}(\Psi, \Delta) = (\Psi_{3n},\Delta_{3n}) - (\Psi_0,\Delta_0)$.

Static SE spectra were analyzed with a five-layer model built with the parameters reported in Table 1.

Broadband SE difference spectra are representative of an average over 30 samples. For each sample an average over 10 static spectra was calculated.

Quartz-Crystal Microbalance with dissipation (QMC-D): QCM-D measurements were performed with a QCM-Z500 (KSV, Finland) microbalance equipped with a thermostated flow chamber. TE buffer (or molecular solutions) was injected into the thermostated prechamber (2 mL) and let to equilibrate at 22 °C for at least 10 min. When fundamental and overtone (3, 5, 7, 9, 11) signals were stable, the solution (about 0.5 mL) was injected into the chamber carefully avoiding microbubble formation (for this reason, buffer was degassed before use and a 0.22 µm filter was employed at the inlet tubing entrance). The responses at fundamental and higher overtones were simultaneously monitored during molecular self-assembly and recorded every 1 s during all experiments. Under the assumption of rigid film formation, the Sauerbrey equation[55,56] was used for the quantification of the adsorbed mass, which is calculated as a function of the sensor's properties as follows

$$\frac{\Delta m}{A} = -C\frac{\Delta f}{n} \tag{3}$$

where $\Delta m/A$ is the adsorbed mass per unit area on the sensor, C is the coefficient that describes the sensitivity of the instrument to changes in mass (for our system: C = 17.7 ng cm^{-2} Hz^{-1}), $\Delta f = f - f_0$ is the shift in frequency and n is the overtone number. Mass/area and

© 2022 The Authors. Advanced Materials Interfaces published by Wiley-VCH GmbH

dissipation changes calculated from the seventh normalized frequency are presented.

QCM-D results are representative of the analysis of 10 samples.

X-ray Photoelectron Spectroscopy (XPS): After the cycle of SE measurements, samples were flushed with Milli-Q, dried under N_2 flow and inserted in a PHI 5600 Multi-Technique apparatus, equipped with an X-ray Al-monochromatized source ($h\nu = 1486.6$ eV) and analyzed. The photoelectron take-off angle was set at 45 degrees. Survey spectra were acquired using a pass-energy of 187.85 eV, while high resolution spectra were acquired with a pass energy of 23.5 eV. For each sample, at least three regions of the sample were considered to check for sample uniformity.

Casa-XPS software was employed for background subtraction from raw data and peak fitting. For the $Au4f_{7/2}$ signal, a Gaussian-Lorentzian asymmetric line shape was used to model the Doniach–Sunjic profile typical of metal surfaces. The binding energy scale was calibrated by setting the $Au4f_{7/2}$ peak at 84.0 eV.

For the other elements, Voigt functions were used for spectral decomposition adopting recommended values for the spin-orbit splitting.

XPS results are representative of the analysis of 30 samples. For each sample an average over the spectra acquired in three different regions was calculated.

Atomic Force Microscopy (AFM): AFM experiments were carried out using a JPK NanoWizard IV microscope (Bruker) in TE buffer. Gold coated Si cantilevers with an elastic constant of 26 N m^{-1} (OTESPA-R3, Bruker) and 0.24 N m^{-1} (DNP-S10, Bruker) were used for shaving and imaging, respectively. Typical forces of hundreds of nN were used for shaving while forces lower than 1 nN were used for imaging.

Data were analyzed with Gwyddion and JPKSPM Data Processing software.

AFM nanolithography results are representative of an average over 10 samples. For each sample at least six shaved regions were analyzed for each deposition step. The semi difference between the highest and lowest film thickness values is reported as the uncertainty of the average film thickness.

Supporting Information

Supporting Information is available from the Wiley Online Library or from the author.

Acknowledgements

The authors thank Loredana Casalis and Pietro Parisse for the introduction to nanoshaving methods, Francesco Bisio and Michele Magnozzi for SE experimental support, and Flavio Gatti for the gold evaporation facility. This work was performed under the project "Dipartimenti di Eccellenza 2017–2022" of the Italian Ministry of Education. Financial support from Università degli Studi di Genova and Italian Ministry of Education (grant RBAP11ETKA-005) is also acknowledged. P.C. and M.C. are not relatives.

Open access funding provided by Universita degli Studi di Genova within the CRUI-CARE Agreement.

Conflict of Interest

The authors declare no conflict of interest.

Data Availability Statement

The data that support the findings of this study are available from the corresponding author upon reasonable request.

Keywords

DNA self-assembled monolayers, hybridization, hypochromism, quartz crystal microbalance, spectroscopic ellipsometry

Received: February 17, 2022
Revised: May 8, 2022
Published online:

[1] S. Yu, T. Chen, Q. Zhang, M. Zhou, X. Zhu, *Analyst* **2020**, *145*, 3481.
[2] S. Takita, A. Nabok, A. Lishchuk, D. Smith, *Int. J. Mol. Sci.* **2021**, *22*, 12701.
[3] A. Al-Jawdah, A. Nabok, H. Abu-Ali, G. Catanante, J.-L. Marty, A. Szekacs, *Anal. Bioanal. Chem.* **2019**, *411*, 7717.
[4] S. Catuogno, C. L. Esposito, C. Quintavalle, L. Cerchia, G. Condorelli, V. De Franciscis, *Cancers* **2011**, *3*, 1877.
[5] D. Chen, Y. Wu, S. Hoque, R. D. Tilley, J. J. Gooding, *Chem. Sci.* **2021**, *12*, 5196.
[6] M. O. Caglayan, Z. Üstündağ, *Spectrochim. Acta, Part A* **2020**, *227*, 117748.
[7] C. M. Niemeyer, T. Sano, C. L. Smith, C. R. Cantor, *Nucleic Acids Res.* **1994**, *22*, 5530.
[8] C. Boozer, J. Ladd, S. Chen, S. Jiang, *Anal. Chem.* **2006**, *78*, 1515.
[9] E. Ambrosetti, P. Paoletti, A. Bosco, P. Parisse, D. Scaini, E. Tagliabue, A. de Marco, L. Casalis, *ACS Omega* **2017**, *2*, 2618.
[10] E. Seymour, G. G. Daaboul, X. Zhang, S. M. Scherr, N. L. Ünlü, J. H. Connor, M. S. Ünlü, *Anal. Chem.* **2015**, *87*, 10505.
[11] Y. Peng, Y. Pan, Z. Sun, J. Li, Y. Yi, J. Yang, G. Li, *Biosens. Bioelectron.* **2021**, *186*, 113309.
[12] C. Hwang, N. Park, E. S. Kim, M. Kim, S. D. Kim, S. Park, N. Y. Kim, J. H. Kim, *Biosens. Bioelectron.* **2021**, *185*, 113177.
[13] A. W. Peterson, R. J. Heaton, R. M. Georgiadis, *Nucleic Acids Res.* **2001**, *29*, 5163.
[14] T. M. Herne, M. J. Tarlov, *J. Am. Chem. Soc.* **1997**, *119*, 8916.
[15] R. Levicky, T. M. Herne, M. J. Tarlov, S. K. Satija, *J. Am. Chem. Soc.* **1998**, *120*, 9787.
[16] R. Lao, S. Song, H. Wu, L. Wang, Z. Zhang, L. He, C. Fan, *Anal. Chem.* **2005**, *77*, 6475.
[17] Y. Song, Y. Liu, M. Yang, B. Zhang, Z. Li, *Appl. Surf. Sci.* **2006**, *252*, 5693.
[18] M. Satjapipat, R. Sanedrin, F. Zhou, *Langmuir* **2001**, *17*, 7637.
[19] P. Gong, C.-Y. Lee, L. J. Gamble, D. G. Castner, D. W. Grainger, *Anal. Chem.* **2006**, *78*, 3326.
[20] P. Vattanaviboon, K. Sangseekhiow, P. Winichagoon, C. Promptmas, *Transl. Res.* **2008**, *151*, 246.
[21] X. C. Zhou, L. Q. Huang, S. F. Y. Li, *Biosens. Bioelectron.* **2001**, *16*, 85.
[22] I. Mannelli, M. Minunni, S. Tombelli, R. Wang, M. M. Spiriti, M. Mascini, *Bioelectrochemistry* **2005**, *66*, 129.
[23] X. Su, Y.-J. Wu, W. Knoll, *Biosens. Bioelectron.* **2005**, *21*, 719.
[24] S. A. J. van der Meulen, G. V. Dubacheva, M. Dogterom, R. P. Richter, M. E. Leunissen, *Langmuir* **2014**, *30*, 6525.
[25] C. Guiducci, C. Stagni, A. Fischetti, U. Mastromatteo, L. Benini, B. Riccoricco, *IEEE Sens. J.* **2006**, *6*, 1084.
[26] L. Wang, M. Veselinovic, L. Yang, B. J. Geiss, D. S. Dandy, T. Chen, *Biosens. Bioelectron.* **2017**, *87*, 646.
[27] S. Cagnin, M. Caraballo, C. Guiducci, P. Martini, M. Ross, M. SantaAna, D. Danley, T. West, G. Lanfranchi, *Sensors* **2009**, *9*, 3122.
[28] M. Trotter, N. Borst, R. Thewes, F. von Stetten, *Biosens. Bioelectron.* **2020**, *154*, 112069.
[29] H.-A. Ho, M. Boissinot, M. G. Bergeron, G. Corbeil, K. Doré, D. Boudreau, M. Leclerc, *Angew. Chem. Int. Ed.* **2002**, *41*, 1548.

© 2022 The Authors. Advanced Materials Interfaces published by Wiley-VCH GmbH

[30] E. Mariotti, M. Minunni, M. Mascini, *Anal. Chim. Acta* **2002**, *8*.
[31] G. Qiu, Z. Gai, Y. Tao, J. Schmitt, G. A. Kullak-Ublick, J. Wang, *ACS Nano* **2020**, *14*, 5268.
[32] K. A. Peterlinz, R. Georgiadis, *Opt. Commun.* **1996**, *130*, 260.
[33] R. M. A. Azzam, N. M. Bashara, *Ellipsometry and Polarized Light*, North-Holland, Amsterdam **1987**.
[34] H. Fujiwara, *Spectroscopic Ellipsometry: Principles and Applications*, John Wiley & Sons, New York **2007**.
[35] K. B. Rodenhausen, T. Kasputis, A. K. Pannier, J. Y. Gerasimov, R. Y. Lai, M. Solinsky, T. E. Tiwald, H. Wang, A. Sarkar, T. Hofmann, N. Ianno, M. Schubert, *Rev. Sci. Instrum.* **2011**, *82*, 103111.
[36] C. Toccafondi, M. Prato, G. Maidecchi, A. Penco, F. Bisio, O. Cavalleri, M. Canepa, *J. Colloid Interface Sci.* **2011**, *364*, 125.
[37] P. Parisse, I. Solano, M. Magnozzi, F. Bisio, L. Casalis, O. Cavalleri, M. Canepa, in *Ellipsometry of Functional Organic Surfaces and Films*, (Eds: K. Hinrichs, K.-J. Eichhorn), Springer International Publishing, Cham **2018**, pp. 63–93.
[38] M. Prato, R. Moroni, F. Bisio, R. Rolandi, L. Mattera, O. Cavalleri, M. Canepa, *J. Phys. Chem. C* **2008**, *112*, 3899.
[39] M. Prato, M. Alloisio, S. A. Jadhav, A. Chincarini, T. Svaldo-Lanero, F. Bisio, O. Cavalleri, M. Canepa, *J. Phys. Chem. C* **2009**, *113*, 20683.
[40] M. Canepa, G. Maidecchi, C. Toccafondi, O. Cavalleri, M. Prato, V. Chaudhari, V. A. Esaulov, *Phys. Chem. Chem. Phys.* **2013**, *15*, 11559.
[41] I. Solano, P. Parisse, F. Gramazio, O. Cavalleri, G. Bracco, M. Castronovo, L. Casalis, M. Canepa, *Phys. Chem. Chem. Phys.* **2015**, *17*, 28774.
[42] C. Toccafondi, O. Cavalleri, F. Bisio, M. Canepa, *Thin Solid Films* **2013**, *543*, 78.
[43] I. Solano, P. Parisse, F. Gramazio, L. Ianeselli, B. Medagli, O. Cavalleri, L. Casalis, M. Canepa, *Appl. Surf. Sci.* **2017**, *421*, 722.
[44] G. Pinto, P. Parisse, I. Solano, P. Canepa, M. Canepa, L. Casalis, O. Cavalleri, *Soft Matter* **2019**, *15*, 2463.
[45] C. Toccafondi, L. Occhi, O. Cavalleri, A. Penco, R. Castagna, A. Bianco, C. Bertarelli, D. Comoretto, M. Canepa, *J. Mater. Chem. C* **2014**, *2*, 4692.
[46] S. Xu, G.-Y. Liu, *Langmuir* **1997**, *13*, 127.
[47] S. H. Brewer, S. J. Anthireya, S. E. Lappi, D. L. Drapcho, S. Franzen, *Langmuir* **2002**, *18*, 4460.
[48] G. Felsenfeld, S. Z. Hirschman, *J. Mol. Biol.* **1965**, *13*, 407.
[49] S. N. Volkov, *Int. J. Quantum Chem.* **1979**, *16*, 119.
[50] R. Thomas, *Gene* **1993**, *135*, 77.
[51] J. J. Nogueira, F. Plasser, L. González, *Chem. Sci.* **2017**, *8*, 5682.
[52] H. Sun, S. Zhang, C. Zhong, Z. Sun, *J. Comput. Chem.* **2016**, *37*, 684.
[53] M. D'Abramo, C. L. Castellazzi, M. Orozco, A. Amadei, *J. Phys. Chem. B* **2013**, *117*, 8697.
[54] S. Elhadj, G. Singh, R. F. Saraf, *Langmuir* **2004**, *20*, 5539.
[55] G. Sauerbrey, *Z. Phys.* **1959**, *155*, 206.
[56] K. Keiji Kanazawa, J. G. Gordon, *Anal. Chem.* **1985**, *57*, 1770.
[57] A. D. Easley, T. Ma, C. I. Eneh, J. Yun, R. M. Thakur, J. L. Lutkenhaus, *J. Polym. Sci.* **2022**, *60*, 1090.
[58] C. Larsson, M. Rodahl, F. Höök, *Anal. Chem.* **2003**, *75*, 5080.
[59] E. Bittrich, K. B. Rodenhausen, K.-J. Eichhorn, T. Hofmann, M. Schubert, M. Stamm, P. Uhlmann, *Biointerphases* **2010**, *5*, 159.
[60] S. Adam, M. Koenig, K. B. Rodenhausen, K.-J. Eichhorn, U. Oertel, M. Schubert, M. Stamm, P. Uhlmann, *Appl. Surf. Sci.* **2017**, *421*, 843.
[61] J. M. Millican, E. Bittrich, A. Caspari, K. Pöschel, A. Drechsler, U. Freudenberg, T. G. Ryan, R. L. Thompson, D. Pospiech, L. R. Hutchings, *Eur. Polym. J.* **2021**, *153*, 110503.
[62] J. Zhang, X. Zhang, X. Wei, Y. Xue, H. Wan, P. Wang, *Anal. Chim. Acta* **2021**, *1164*, 338321.
[63] D. Y. Petrovykh, H. Kimura-Suda, M. J. Tarlov, L. J. Whitman, *Langmuir* **2004**, *20*, 429.
[64] A. Opdahl, D. Y. Petrovykh, H. Kimura-Suda, M. J. Tarlov, L. J. Whitman, *Proc. Natl. Acad. Sci. USA* **2007**, *104*, 9.
[65] M. R. Vilar, A. M. Botelho do Rego, A. M. Ferraria, Y. Jugnet, C. Noguès, D. Peled, R. Naaman, *J. Phys. Chem. B* **2008**, *112*, 6957.
[66] A. B. Steel, R. L. Levicky, T. M. Herne, M. J. Tarlov, *Biophys. J.* **2000**, *79*, 975.
[67] Z. Li, T. Niu, Z. Zhang, R. Chen, G. Feng, S. Bi, *Biosens. Bioelectron.* **2011**, *26*, 4564.
[68] M. N. Khan, M. Zharnikov, *J. Phys. Chem. C* **2014**, *118*, 3093.
[69] C. Vericat, M. E. Vela, G. Benitez, P. Carro, R. C. Salvarezza, *Chem. Soc. Rev.* **2010**, *39*, 1805.
[70] Z. Li, T. Niu, Z. Zhang, G. Feng, S. Bi, *Analyst* **2012**, *137*, 1680.
[71] J. M. Berg, J. L. Tymoczko, G. J. Gatto, L. Stryer, *Biochemistry*, W.H. Freeman & Company, New York **2015**.
[72] H. Hamoudi, M. Prato, C. Dablemont, O. Cavalleri, M. Canepa, V. A. Esaulov, *Langmuir* **2010**, *26*, 7242.
[73] G. Pinto, P. Canepa, C. Canale, M. Canepa, O. Cavalleri, *Materials* **2020**, *13*, 2888.
[74] A. Rich, M. Kasha, *J. Am. Chem. Soc.* **1960**, *82*, 6197.
[75] R. G. Nuzzo, B. R. Zegarski, L. H. Dubois, *J. Am. Chem. Soc.* **1987**, *109*, 733.
[76] P. E. Laibinis, G. M. Whitesides, D. L. Allara, Y. T. Tao, A. N. Parikh, R. G. Nuzzo, *J. Am. Chem. Soc.* **1991**, *113*, 7152.
[77] D. G. Castner, K. Hinds, D. W. Grainger, *Langmuir* **1996**, *12*, 5083.
[78] M. Zharnikov, M. Grunze, *J. Phys.: Condens. Matter* **2001**, *13*, 11333.
[79] C. Vericat, M. E. Vela, G. Andreasen, R. C. Salvarezza, L. Vázquez, J. A. Martín-Gago, *Langmuir* **2001**, *17*, 4919.
[80] G. Gonella, S. Terreni, D. Cvetko, A. Cossaro, L. Mattera, O. Cavalleri, R. Rolandi, A. Morgante, L. Floreano, M. Canepa, *J. Phys. Chem. B* **2005**, *109*, 18003.
[81] O. Cavalleri, G. Gonella, S. Terreni, M. Vignolo, P. Pelori, L. Floreano, A. Morgante, M. Canepa, R. Rolandi, *J. Phys.: Condens. Matter* **2004**, *16*, S2477.
[82] L. G. Carrascosa, L. Martínez, Y. Huttel, E. Román, L. M. Lechuga, *Eur. Biophys. J.* **2010**, *39*, 1433.
[83] H. Wang, M. Liu, W. Bai, H. Sun, Y. Li, H. Deng, *Sens. Actuators, B* **2019**, *284*, 236.
[84] C. Vericat, M. E. Vela, G. Corthey, E. Pensa, E. Cortés, M. H. Fonticelli, F. Ibañez, G. E. Benitez, P. Carro, R. C. Salvarezza, *RSC Adv.* **2014**, *4*, 27730.
[85] K. Kummer, D. V. Vyalikh, G. Gavrila, A. Kade, M. Weigel-Jech, M. Mertig, S. L. Molodtsov, *J. Electron Spectrosc. Relat. Phenom.* **2008**, *163*, 59.
[86] A. Kick, M. Bönsch, K. Kummer, D. V. Vyalikh, S. L. Molodtsov, M. Mertig, *J. Electron Spectrosc. Relat. Phenom.* **2009**, *172*, 36.
[87] D. Grumelli, F. L. Maza, K. Kern, R. C. Salvarezza, P. Carro, *J. Phys. Chem. C* **2016**, *120*, 291.
[88] O. Cavalleri, L. Oliveri, A. Daccà, R. Parodi, R. Rolandi, *Appl. Surf. Sci.* **2001**, *175*, 357.
[89] O. Cavalleri, G. Gonella, S. Terreni, M. Vignolo, L. Floreano, A. Morgante, M. Canepa, R. Rolandi, *Phys. Chem. Chem. Phys.* **2004**, *6*, 4042.
[90] Y. W. Yang, L. J. Fan, *Langmuir* **2002**, *18*, 1157.
[91] M. Zharnikov, *J. Electron Spectrosc. Relat. Phenom.* **2010**, *178–179*, 380.
[92] J. R. Krivacic, D. W. Urry, *Anal. Chem.* **1970**, *42*, 596.
[93] T. Berlind, G. K. Pribil, D. Thompson, J. A. Woollam, H. Arwin, *Phys. Status Solidi C* **2008**, *5*, 1249.
[94] S. D. Silaghi, M. Friedrich, C. Cobet, N. Esser, W. Braun, D. R. T. Zahn, *Phys. Status Solidi B* **2005**, *242*, 3047.

© 2022 The Authors. Advanced Materials Interfaces published by Wiley-VCH GmbH

[95] K. Hinrichs, S. D. Silaghi, C. Cobet, N. Esser, D. R. T. Zahn, *Phys. Status Solidi B* **2005**, *242*, 2681.
[96] J. Maartensson, H. Arwin, *Langmuir* **1995**, *11*, 963.
[97] T. Inagaki, R. N. Hamm, E. T. Arakawa, L. R. Painter, *J. Chem. Phys.* **1974**, *61*, 4246.
[98] A. Ito, T. Ito, *Photochem. Photobiol.* **1986**, *44*, 355.
[99] S. Wenmackers, S. D. Pop, K. Roodenko, V. Vermeeren, O. A. Williams, M. Daenen, O. Douhéret, J. D'Haen, A. Hardy, M. K. Van Bael, K. Hinrichs, C. Cobet, M. vandeVen, M. Ameloot, K. Haenen, L. Michiels, N. Esser, P. Wagner, *Langmuir* **2008**, *24*, 7269.
[100] W. Jung, H. Jun, S. Hong, B. Paulson, Y. S. Nam, K. Oh, *Opt. Mater. Express* **2017**, *7*, 3796.
[101] N.d.
[102] X. Wang, H. J. Lim, A. Son, *Environ. Health Toxicol.* **2014**, *29*, 8.
[103] A. W. Peterson, *Nucleic Acids Res.* **2001**, *29*, 5163.

© 2022 The Authors. Advanced Materials Interfaces published by Wiley-VCH GmbH